

Elastic  $\alpha$  Angular Distributions in the Sharp Cutoff Model\*

J. S. BLAIR

*Department of Physics, University of Washington, Seattle, Washington*

(Received July 19, 1957)

An analysis is made in terms of a semiclassical strong absorption model of all published angular distributions of intermediate energy alpha particles elastically scattered from heavy or medium weight nuclei as well as some examples of elastic proton and deuteron scattering. Moderately good agreement is found for radii obtained from different sets of data and also from analysis of fixed angle, variable energy experiments; there is some indication that the sharp cutoff radius increases as the bombarding energy is lowered to the Coulomb barrier. The connection between these results and optical model parameters is discussed. The best-fit critical angular momenta,  $l'$ , are found to be essentially equivalent to the largest angular momenta,  $l_m$ , such that the  $l_m$ th potential barrier is classically surmounted by the bombarding particle when the most recent optical model parameters are used to represent the nuclear potential. It is suggested that, when the penetration depth is small, the most important "effective" parameter is  $l_m$ .

## I. INTRODUCTION

CONSIDERABLE experimental information has been obtained in recent years on the elastic scattering of intermediate energy (10–50 Mev) alpha particles by nuclei; cross sections have been measured as a function of energy at fixed scattering angles<sup>1,2</sup> and as a function of angle at fixed energy.<sup>3–11</sup> The measurements at fixed angle and some of the angular distributions<sup>3,5,6</sup> have been analyzed in terms of a semiclassical strong absorption model (henceforth termed the sharp cutoff model)<sup>12,13</sup> or "fuzzy" modifications of this model.<sup>3,6</sup> Improved agreement with the data is obtainable with optical model calculations<sup>14,15</sup> and, in particular, recent results obtained with the aid of high-speed digital computers have reproduced experimental angular distributions to a high degree of precision.<sup>16–19</sup>

Angular distributions computed with the sharp cutoff model for heavy elements reproduce the observed break from pure Coulomb scattering, the average slope in a region down to  $\sim \frac{1}{5}$  Coulomb and the initial rise

seen in many elements. The computed curves, however, do not match the continuing downward experimental curves; further, "diffraction" oscillations either are not observed at all or have a smaller magnitude than predicted. An extensive discussion of the range of applicability of the sharp cutoff model, and some of the factors determining the initial rise and diffraction oscillations, is presented elsewhere.<sup>13</sup>

The purpose of the present note is (a) to discuss all published intermediate-energy elastic- $\alpha$  angular distributions from heavy and medium weight nuclei in terms of the sharp cutoff model as well as to apply this model to some examples of elastic deuteron<sup>7,8</sup> and proton<sup>20</sup> scattering, and (b) to compare the results of this analysis with the parameters of optical model calculations.

## II. ANALYSIS OF EXPERIMENTS

The chief assumption of the sharp cutoff model is that the amplitude of the outgoing  $l$ th partial wave is set equal to zero for  $\hbar l$  less than or equal to a critical angular momentum,  $\hbar l'$ ; if  $l > l'$ , the outgoing amplitude takes on the value it has for pure Coulomb scattering.<sup>12</sup> The critical angular momentum,  $\hbar l'$ , is assumed to be that angular momentum for which the projectile can classically just penetrate the nuclear interior. For the case of a nucleus described by a square-well potential, the critical angular momentum may be accordingly related to the sharp cutoff radius  $R$ , through

$$E = ZZ'e^2/R + \hbar^2 l'(l'+1)/(2\mu R^2). \quad (1)$$

The model contains but one free parameter,  $l'$ , or its equivalent,  $R$ . The computations of the resulting angular distributions have been performed on the University of Washington IBM 604 electronic computer.

Best-fit radii can be obtained in cases where oscillations are not present or are greatly damped through (a) comparison of computed and experimental angular distributions in the vicinity of the break from Coulomb

\* Supported in part by the U. S. Atomic Energy Commission.

<sup>1</sup> G. W. Farwell and H. E. Wegner, Phys. Rev. **93**, 356 (1954).

<sup>2</sup> G. W. Farwell and H. E. Wegner, Phys. Rev. **95**, 1212 (1954).

<sup>3</sup> Wall, Rees, and Ford, Phys. Rev. **97**, 726 (1955).

<sup>4</sup> Wegner, Eisberg, and Igo, Phys. Rev. **99**, 825 (1955).

<sup>5</sup> R. Ellis and L. Schechter, Phys. Rev. **99**, 1044 (1955).

<sup>6</sup> R. Ellis and L. Schechter, Phys. Rev. **101**, 636 (1956).

<sup>7</sup> H. E. Gove, Massachusetts Institute of Technology, Laboratory for Nuclear Science and Engineering Progress Report, July 1, 1950, p. 139; February 28, 1951, p. 40.

<sup>8</sup> H. E. Gove, Phys. Rev. **99**, 1353 (1955).

<sup>9</sup> Eisberg, Igo, and Wegner, Phys. Rev. **99**, 1606 (1955).

<sup>10</sup> E. Bleuler and D. J. Tendam, Phys. Rev. **99**, 1605 (1955).

<sup>11</sup> Igo, Wegner, and Eisberg, Phys. Rev. **101**, 1508 (1956).

<sup>12</sup> J. S. Blair, Phys. Rev. **95**, 1218 (1954).

<sup>13</sup> Kerlee, Blair, and Farwell, Phys. Rev. **107**, 1343 (1957).

<sup>14</sup> N. Oda and K. Harada, Progr. Theoret. Phys. Japan **15**, 545 (1956).

<sup>15</sup> C. B. O. Mohr and B. A. Robson, Proc. Phys. Soc. (London) **A69**, 365 (1956).

<sup>16</sup> W. B. Cheston and A. E. Glassgold, Bull. Am. Phys. Soc. Ser. II, **1**, 339 (1956).

<sup>17</sup> Igo, Thaler, and Hill, Bull. Am. Phys. Soc. Ser. II, **1**, 384 (1956).

<sup>18</sup> W. B. Cheston and A. E. Glassgold, Phys. Rev. **106**, 1215 (1957).

<sup>19</sup> G. Igo and R. M. Thaler, Phys. Rev. **106**, 126 (1957).

<sup>20</sup> I. E. Dayton and G. Schranck, Phys. Rev. **101**, 1358 (1956).

TABLE I. Best-fit  $l'$  and radii. The best-fit  $R$  is related to  $l'$  through Eq. (1).  $dR$  is the change in  $R$  for  $\Delta l = 1$ . The classical parameter,  $n$ , is defined as  $n \equiv (ZZ'e^2/\hbar v)$ .

Element	Projectile	Nuclear charge	Reference	$E_{c.m.}$ in Mev	$n$	Best $l'$	Best-fit $R$ in $10^{-13}$ cm	$dR$ in $10^{-13}$ cm
Th	$\alpha$	90	4	39.3	8.96	18	10.85	0.34
			13	34.09			11.02 $\pm$ 0.23	
Pb	$\alpha$	82	3	21.58	11.01	4	11.38	0.19
			4	39.2	8.17	18	10.46	0.34
			6	47.3	7.44	21-22	10.12-10.44	0.32
			13	32.7			10.47 $\pm$ 0.21	
			8	14.91	4.70	6	10.71	0.79
Au	$\alpha$	79	3	21.56	10.61	4-5	11.00-11.20	0.20
			4	39.2	7.87	18	10.31	0.34
			6	47.2	7.19	22	10.33	0.31
			8	26.95	9.49	11	10.85	0.34
			13	31.68			10.42 $\pm$ 0.21	
Ta	$p$	73	20	17.0	3.01	3	8.44	0.89
			4	39.1	7.27	20	10.71	0.35
Ag	$\alpha$	47	13	38			10.07 $\pm$ 0.2	
			3	21.21	6.31	10	9.38	0.43
			6	46.5	4.27	21-23	8.92-9.59	0.36
			11	38.6	4.68	19	9.26	0.36
			13	21.91			8.94 $\pm$ 0.18	
Mo	$p$	42	20	17.0	1.79	3-4	6.32-7.35	1.03
			11	38.4	4.18	18	8.72	0.37
Nb	$\alpha$	41	11	38.4	4.08	18	8.67	0.37
Cu	$\alpha$	29	10	17.8	4.20	9	8.15	0.52
			11	37.6	2.89	18	8.32	0.41
			13	22.7			7.81	
Ti	$\alpha$	22	11	36.9	2.19	16	7.38	0.39

and (b) the "crossover" point recipe discussed elsewhere,<sup>13</sup> which supplants the previous one-quarter-point recipe.<sup>12</sup> When oscillations are present, their location and spacing also are used to determine the best fits.

The best  $l'$  and corresponding  $R$ , as well as values of the classical parameter  $n$  ( $\equiv ZZ'e^2/\hbar v$ ) are tabulated in Table I. In many cases, a best  $l'$  can be assigned quite unambiguously; unless otherwise stated, the error in  $R$  is conservatively estimated by  $dR$ , the change in  $R$  when  $l'$  is changed by 1. For the heavier elements, the values of  $R$  obtained from application of the crossover recipe to fixed-angle measurements<sup>13</sup> are also presented as well as the center-of-mass energy at which cross over occurred. Radii computed from the crossover recipe and the best-fit radii for the same angular data are given in Table II. Specific comments on the data and their analysis are made below in order of reference.

Wall, Rees, and Ford<sup>3</sup>—22-Mev  $\alpha$  on Pb, Au, Ag.

TABLE II. Best-fit and crossover radii for the same angular distribution.

Element	Projectile	Reference	Best-fit $R$ in $10^{-13}$ cm	$dR$	Crossover $R$ in $10^{-13}$ cm
Th	$\alpha$	4	10.85	0.34	11.01 $\pm$ 0.1
Pb	$\alpha$	4	10.46	0.34	10.71 $\pm$ 0.1
		6	10.12, 10.44	0.32	10.59 $\pm$ 0.3
Au	$\alpha$	8	10.71	0.79	9.71 $\pm$ 0.2
		4	10.31	0.34	10.49 $\pm$ 0.1
		6	10.33	0.31	10.57 $\pm$ 0.3
		8	10.85	0.34	10.63 $\pm$ 0.1
		4	10.71	0.35	10.79 $\pm$ 0.1
Ta	$\alpha$	3	9.38	0.43	9.54 $\pm$ 0.2
Ag	$\alpha$	11	9.26	0.36	8.67 $\pm$ 0.2

This reference contains an analysis in terms of the sharp cutoff model and a "fuzzy" modification. The values of  $R$  in Table I are somewhat different from those quoted in reference 3 since we are comparing experiments only to the sharp-cutoff calculations and we include some small center-of-mass corrections. The cross sections of Pb and Au do not fall far enough below Coulomb for the crossover recipe to be employed.

Wegner, Eisberg, and Igo<sup>4</sup>—40-Mev  $\alpha$  on Th, Pb, Au, and Ta. The computed angular distributions provide a fairly good fit of the initial rise and the general trend just below the break for Th, Pb, and Au; the angular distribution from Th for the best fit,  $l' = 18$ , is shown in Fig. 1. The radius here determined for Ta is substantially larger than that found in fixed angle experiments<sup>13</sup>; in Fig. 2 it is seen that the computed location of the initial rise in Ta is around 20°. Since the experimental angular distributions have been normalized to Coulomb at 21°, it is likely that the experimental plot of  $\sigma/\sigma_C$  for Ta is low by 10-20%; a change of that order of magnitude suffices to bring the Ta radius into agreement with the radius reported in reference 13. The values of  $n$  for which the computations of  $\sigma/\sigma_C$  are carried out are about 1% below the experimental values; such a small shift in  $n$  does not change our assignment of best  $l'$  (see reference 3, Fig. 5).

Ellis and Schechter<sup>5,6</sup>—48-Mev  $\alpha$  on Pb, Au, and Ag. The best computed curves exhibit oscillations whose spacing and location closely match the experimental results. Indeed, the computed angular distribution for Pb with  $l' = 21$ , Fig. 3(a), shows the observed "dimple" in the initial rise. The experimental angular distribution

from Au also oscillates slightly; this variation is particularly noticeable when experiment is compared to the computed cross section for  $l'=22$ , Fig. 4. There is a sizeable uncertainty in assigning the best fit for Ag;

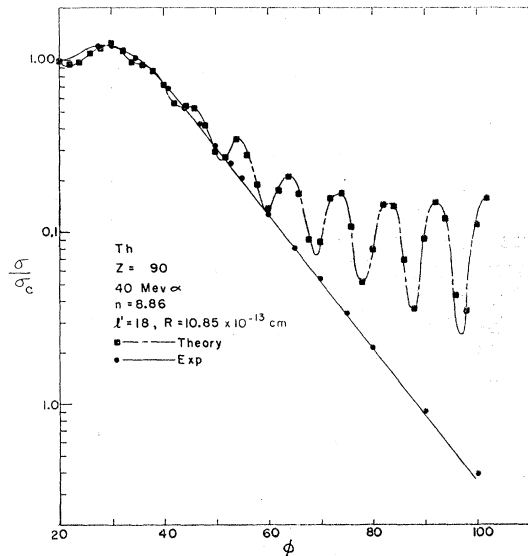


FIG. 1. Angular distribution of 40-Mev alpha particles from Th relative to the pure Coulomb cross section. The solid curve and dots represent the data of Wegner, Eisberg, and Igo. The dotted curve and squares represent the computed angular distribution with  $l'=18$ ,  $R=10.85 \times 10^{-13}$  cm. Experimental data are plotted *versus* laboratory scattering angle while the computed points are for center-of-mass scattering angle.

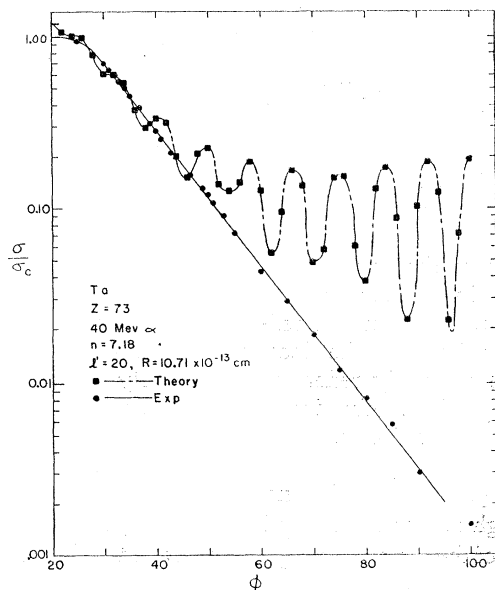
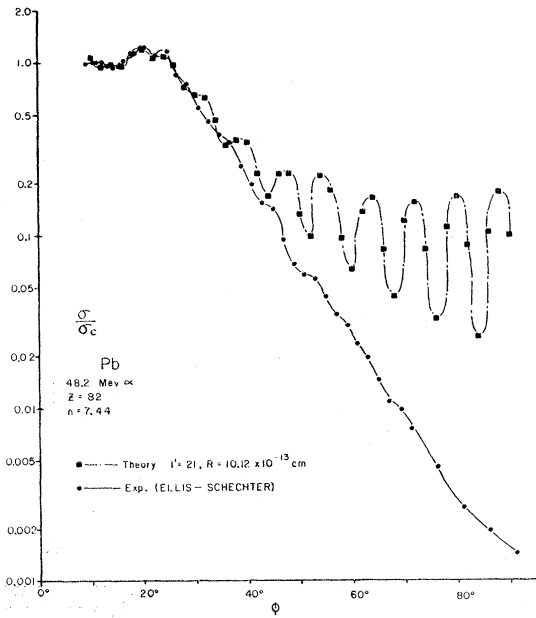
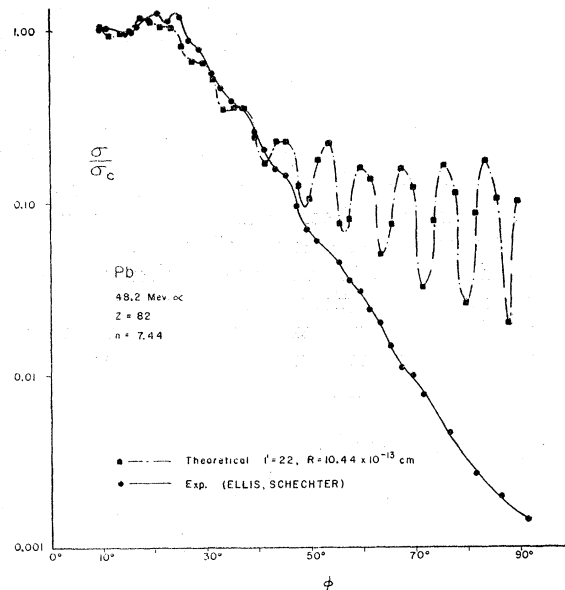


FIG. 2. Angular distribution of 40-Mev alpha particles from Ta relative to the pure Coulomb cross section. The solid curve and dots represent the data of Wegner, Eisberg, and Igo. The dotted curve and squares represent the computed angular distribution with  $l'=20$ ,  $R=10.71 \times 10^{-13}$  cm. Experimental data are plotted *versus* laboratory scattering angle while the computed points are for center-of-mass scattering angle.



(a)



(b)

FIG. 3. Angular distribution of 48.2-Mev alpha particles from Pb relative to the pure Coulomb cross section. The solid curve and dots represent the experimental data of Ellis and Schechter. The data actually extend to larger angles than here shown; the points drop about another decade and then, within rather large probable errors, show a small rise. The dotted curves and squares represent the computed angular distribution; in Fig. 3(a),  $l'=21$ ,  $R=10.12 \times 10^{-13}$  cm, in Fig. 3(b),  $l'=22$ ,  $R=10.44 \times 10^{-13}$  cm.  $\phi$  is the center-of-mass scattering angle.

$l'=21$  produces the correct location of the oscillations while  $l'=23$  best describes the cross section in the neighborhood of the break. Agreement between experiment and the sharp cutoff calculations of course becomes poorer as  $Z$  is decreased since the semiclassical model is

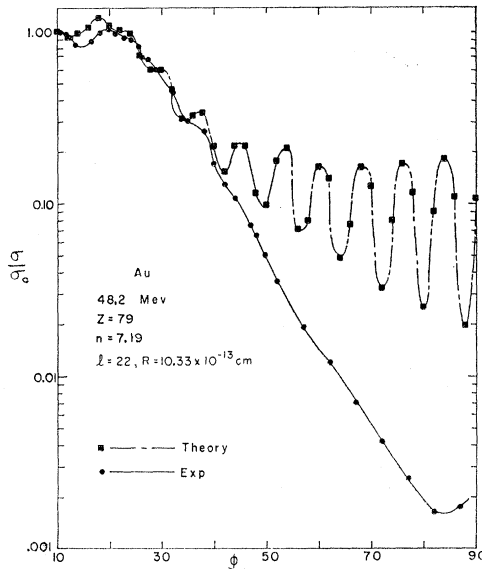


FIG. 4. Angular distribution of 48.2-Mev alpha particles from Au relative to the pure Coulomb cross section. The solid curve and dots represent the experimental data of Ellis and Schechter. The data actually extend to larger angles than here shown; the points drop about another decade and then show a slight rise. The dotted curve and squares represent the computed angular distribution for  $l'=22$ ,  $R=10.33 \times 10^{-13}$  cm.  $\phi$  is the center-of-mass scattering angle.

most valid for large values of the "classical" parameter,  $n \equiv (ZZ'e^2/\hbar v)$ . We feel that the somewhat improved agreement brought about by the modified sharp cutoff model of Ellis and Schechter is not great enough to justify the considerable extra effort that would be required if we were to introduce another parameter,  $\Delta l$ , into our computations; further, one would then lose one of the chief virtues of the sharp cutoff model, that it depends on but a single free parameter.

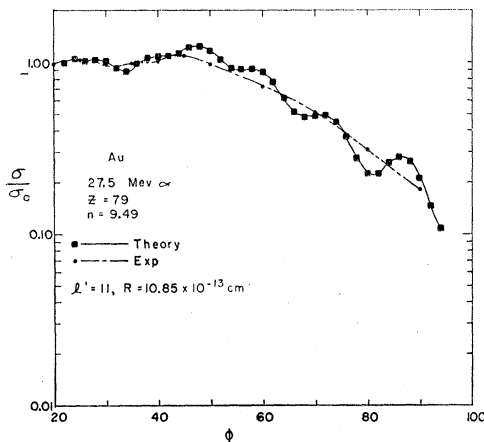


FIG. 5. Angular distribution of 27.5-Mev alpha particles from Au relative to the pure Coulomb cross section. The solid curve and dots represent the data of Gove. The dotted curve and squares represent the computed angular distribution with  $l'=11$ ,  $R=10.85 \times 10^{-13}$  cm. Experimental data are plotted versus laboratory scattering angle while the computed points are for center-of-mass scattering angle.

Gove<sup>7,8</sup>—27.5-Mev  $\alpha$  on Au. Figure 5 indicates that the data are well straddled by the computed curve for  $l'=11$ . The parameter  $n$  and scattering angle near the break are larger than was the case in the preceding paragraph; in view of the discussion of fine structure in reference 13 it is not surprising, then, that the diffraction oscillations are apparently washed out.

15.2-Mev  $d$  on Pb. For once the envelope of the computed curve falls off faster than does experiment, as shown in Fig. 6. The discrepancy between best-fit and crossover radii and the large value for  $dR$  suggest that these radii should not be taken too seriously. There is some indication in the observed angular distribution of the predicted oscillations.

Eisberg, Igo, and Wegner<sup>9,11</sup>—40-Mev  $\alpha$  on Ag, Mo, Nb, Cu, Ti. For this range of  $n$  there is poor agreement with the observed magnitudes even at the smaller angles. Nonetheless it is interesting to see that reasonable  $l'$  fit the spacing and location of the maxima and

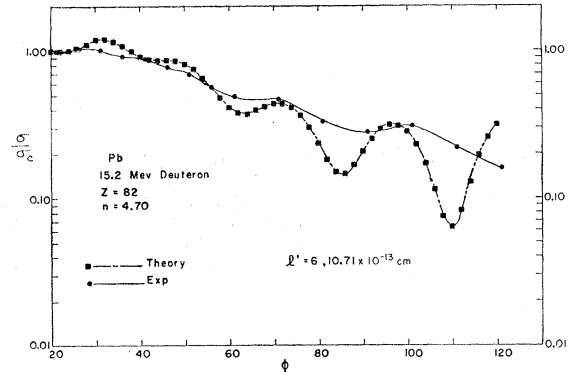


FIG. 6. Angular distribution of 15.2-Mev deuterons from Pb relative to the pure Coulomb cross section. The solid curve and dots represent the data of Gove. The dotted curve and squares represent the computed angular distribution with  $l'=6$ ,  $R=10.71 \times 10^{-13}$  cm. Experimental data are plotted versus laboratory scattering angle while the computed points are for center-of-mass scattering angle.

minima of the oscillations. This is illustrated for the case of Nb,  $l'=18$ , in Fig. 7 and for Cu,  $l'=18$ , in Fig. 8. As treated more fully in reference 13, such agreement is possible because the location of the maxima and minima primarily reflect the periodicity in the oscillations of the amplitudes for pure Coulomb scattering as a function of  $l$ . Once again we have a situation familiar from physical optics where a crude physical model correctly predicts the location of diffraction structure although it incorrectly predicts the magnitude. Application of the crossover recipe to the Ag data is hazardous in view of the large oscillations.

Bleuler and Tendam<sup>10</sup>—18.9-Mev  $\alpha$  on Cu. The comparison in Fig. 9 reveals that fair agreement with the magnitude of the cross section at small angles (as well as correct predictions of the location of oscillations) is achieved with the choice  $l'=9$ .

Dayton and Shranck<sup>20</sup>—17-Mev protons on Au and Ag. The angular distribution from Au is presented in Fig. 10 to show that some of the quantitative features of proton scattering are duplicated by the crude one-parameter sharp cutoff model. Even though protons are the bombarding particles, the parameter  $n$  is large enough so that the semiclassical treatment has some meaning. The best-fit radius,  $8.44 \times 10^{-13}$  cm is smaller than the radius obtained with  $\alpha$  scattering by an amount substantially greater than the probable errors.

In summary, we may say that, wherever comparison is possible, there is fairly good consistency between the sharp cutoff radii obtained in alpha scattering from the

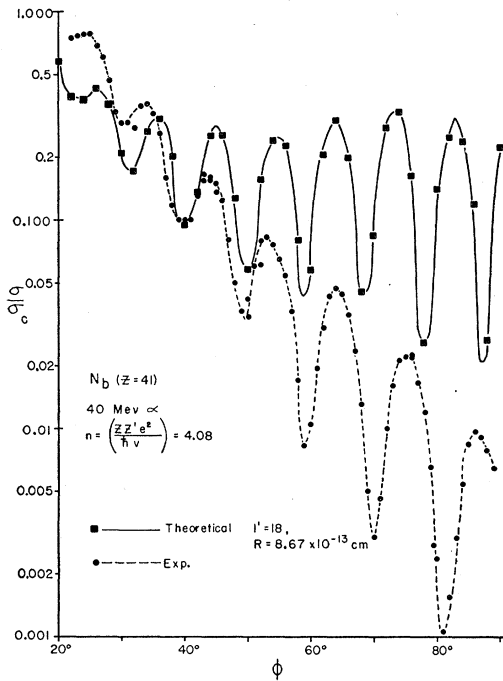


FIG. 7. Angular distribution of 40-Mev alpha particles from Nb relative to the pure Coulomb cross section. The solid curve and dots represent the data of Igo, Wegner, and Eisberg. The dotted curve and squares represent the computed angular distribution with  $l'=18$ ,  $R=8.67 \times 10^{-13}$  cm.  $\phi$  is the center-of-mass angle.

same element. However, the data of Wall *et al.* on Pb and Au and Gove on Au at energies close to the Coulomb barrier do yield larger radii than do other determinations.

### III. COMPARISON WITH OPTICAL MODEL RESULTS

In this section we will attempt to answer three questions which rather naturally come to mind: (1) what is the connection between the sharp cutoff momentum  $l'$  and the parameters of the optical model calculation? (2) Why should the sharp cutoff model be a good approximation to the optical model? (3) What lessons may be drawn from the comparison?

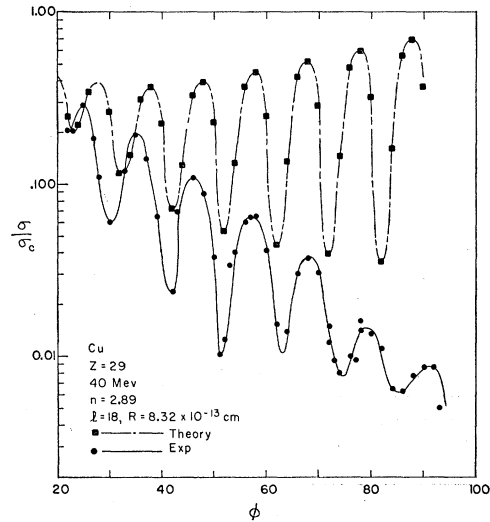


FIG. 8. Angular distribution of 40-Mev alpha particles from Cu relative to the pure Coulomb cross section. The solid curve and dots represent the data of Igo, Wegner, and Eisberg. The dotted curve and squares represent the computed angular distribution with  $l'=18$ ,  $R=8.32 \times 10^{-13}$  cm.  $\phi$  is the center-of-mass scattering angle.

(1) At first sight the sharp cutoff and optical results appear to be incompatible in that the sharp-cutoff radii are considerably larger than the mean radii of the nuclear potential.<sup>16-19</sup> The discrepancy is only apparent, however, since the two radii are quite differently defined. We can relate these two radii by noting again the basic assumption of the sharp cutoff model and applying it to the tapered-well optical potentials which give the best fit. The critical angular momentum,  $\hbar l'$ , is assumed to be such that the projectile can classically just override the potential barrier into the nucleus. If we have a deep nuclear potential with a "tail," the critical classical turning point is not located at the mean radius but rather is found at a distance several "surface thicknesses" beyond the mean radius, depending on the strength of the potential, with correspondingly large  $l'$ .

To illustrate this point, we consider the familiar Saxon-Woods<sup>21</sup> optical potential in the case of alphas with 38.6-Mev c.m. energy scattered on Ag. The best values of the optical parameters quoted by Igo and Thaler<sup>19</sup> are: the real part of potential at center of nucleus,  $V_R = -37$  Mev; the imaginary part,  $V_I = -10$  Mev; mean radius,  $r_1 = (1.35A^{1/3} + 1.3) \times 10^{-13}$  cm =  $7.73 \times 10^{-13}$  cm; surface parameter,  $d = 0.5 \times 10^{-13}$  cm. When the real part of total potential including nuclear, Coulomb, and centrifugal terms is plotted *versus*  $r$ , as shown in Fig. 11, it is found that  $l_m$ , the largest angular momentum such that the classical barrier is safely surmounted, is equal to 19. The top of the  $l_m$ th barrier occurs at  $r_b = 8.7 \times 10^{-13}$  cm. (We see from Table I that  $l'=19$  also gives the best fit of the sharp cutoff model,

<sup>21</sup> R. D. Woods and D. S. Saxon, Phys. Rev. **95**, 577 (1954).

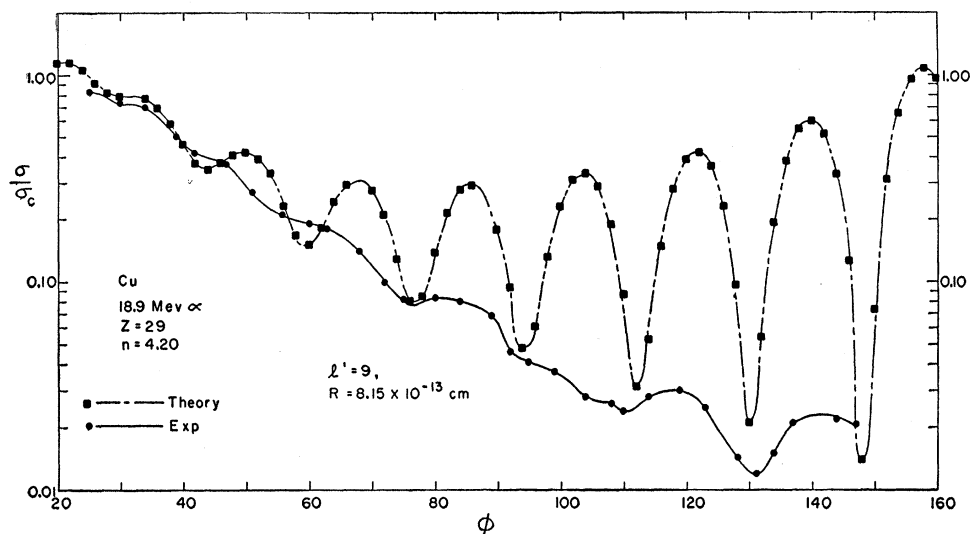


FIG. 9. Angular distribution of 18.9-Mev alpha particles on Cu relative to the pure Coulomb cross section. The solid curve and dots represent the data of Bleuler and Tendam. The dotted curve and squares represent the computed angular distribution with  $l'=9$ ,  $R=8.15 \times 10^{-13}$  cm.  $\phi$  is the center-of-mass scattering angle.

with corresponding sharp cutoff radius equal to  $9.26 \times 10^{-13}$  cm.)

The largest angular momentum,  $l_m$ , such that the total barrier is surmounted by at least 0.1 Mev can be similarly obtained for other elements where the optical parameters are given.<sup>13,19</sup> These are listed in Table III together with  $R_m$ , the sharp-cutoff radius corresponding to  $l_m$ ;  $r_b$ , the radius at which the  $l_m$ th potential is a maximum;  $-V_R(r_b)$ , the nuclear potential at  $r_b$ ; the best-fit  $l'$  from Table I and corresponding sharp-cutoff radius,  $R$ . This determination of  $l_m$  has not biased our selection of the best-fit  $l'$  since the best-fit analyses were carried out before the optical parameters became

available. Inspection of Table III shows that  $l'$  and  $l_m$  generally agree or differ by only one unit of angular momentum.

In the case of 22-Mev scattering from Ag, three quite different sets of optical parameter are available which fit the data: Igo and Thaler find  $V_R = -35$  Mev,  $r_1 = 7.73 \times 10^{-13}$  cm,  $d = 0.5 \times 10^{-13}$  cm, while Cheston and Glassgold obtain adequate fits with both  $V_R = -50$  Mev,  $r_1 = 7.5 \times 10^{-13}$  cm,  $d = 0.6 \times 10^{-13}$  cm, and  $V_R = -150$  Mev,  $r_1 = 7.09 \times 10^{-13}$  cm,  $d = 0.6 \times 10^{-13}$  cm. (There is apparently some disagreement on this point; Igo and Thaler<sup>19</sup> do not find appreciable change in  $V_R$  if  $r_1$  is changed.) The spread in  $l_m$  quoted for these cases

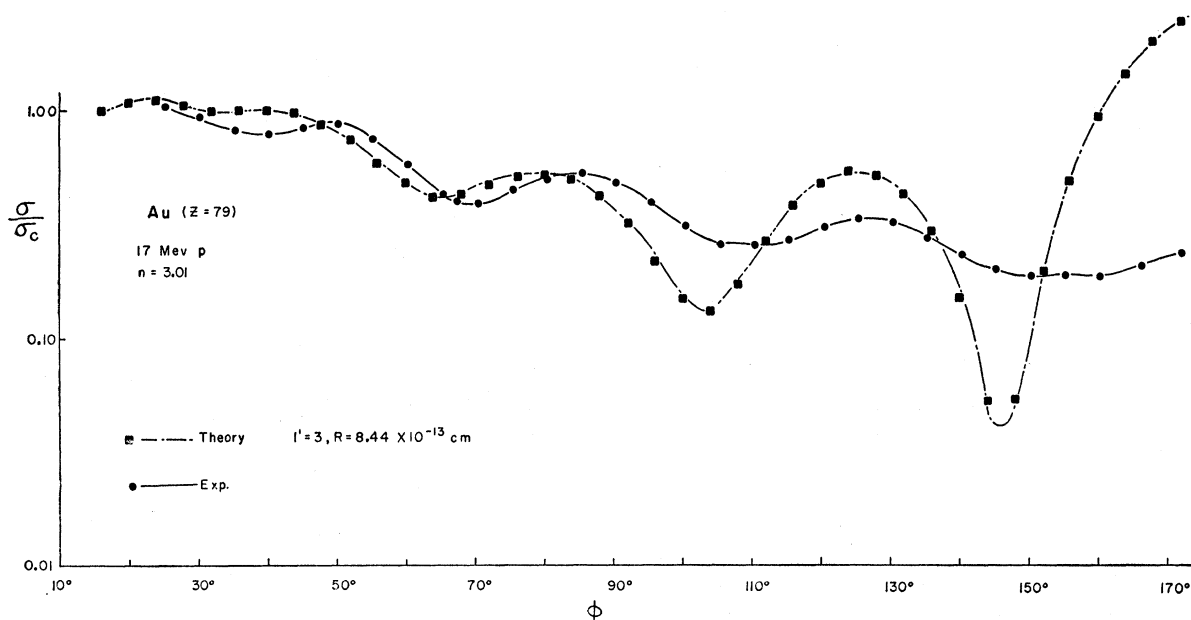


FIG. 10. Angular distribution of 17-Mev protons from Au relative to the pure Coulomb cross section. The solid curve and dots represent the data of Dayton and Shranck. The dotted curve and squares represent the computed angular distribution with  $l'=3$ ,  $R=8.44 \times 10^{-13}$  cm.  $\phi$  is the center-of-mass scattering angle.

TABLE III. Comparison of best-fit  $V$  and  $R$  to  $l_m$ , the largest angular momentum such that the optical potential barrier is surmounted by at least 0.1 Mev;  $r_b$ , the radius at which the  $l_m$ th barrier is a maximum;  $R_m$ , the sharp-cutoff radius corresponding to  $l_m$ ;  $-V_R(r_b)$ , the magnitude of the real part of the nuclear potential at the top of the barrier. Unless otherwise stated, the optical parameters chosen are those of Igo and Thaler.<sup>a</sup>

Element	Reference	$E_{c.m.}$ in Mev	$l_m$	$r_b$ $10^{-13}$ cm	$R_m$ $10^{-13}$ cm	$l'$	$R$ $10^{-13}$ cm	$-V_R(r_b)$
Ti	11	36.9	16	6.7	7.38	16	7.38	8.1
Cu	11	37.6	18	7.7	7.91	19	8.32	5.3
Nb	11	38.4	19	8.5	9.04	18	8.67	4.6
Mo	11	38.4	19	8.5	9.10	18	8.72	4.9
Ag	3	21.21 <sup>b</sup>	10	9.2	9.38	10	9.38	1.8
Ag	3	21.21 <sup>c</sup>	11	9.4	9.81			2.0
Ag	3	21.21 <sup>d</sup>	12	9.6	10.26			2.2
Ag	11	38.6	19	8.7	9.26	19	9.26	4.7
Ta	4	39.1	20	10.3	10.71	20	10.71	3.2
Au	3	21.56	5	10.8	11.20	4-5	11.00-11.20	1.1
Au	4	39.2	19	10.5	10.65	18	10.31	2.8
Pb	3	21.58	4	10.9	11.38	4	11.38	1.2
Pb	4	39.2	19	10.6	10.80	18	10.46	2.9
Th	4	39.3	19	11.0	11.19	18	10.85	2.4

<sup>a</sup> See reference 19.

<sup>b</sup> Igo and Thaler,  $V_R = -35$  Mev,  $r_1 = 7.73 \times 10^{-13}$  cm,  $d = 0.5 \times 10^{-13}$  cm.

<sup>c</sup> Cheston and Glassgold,  $V_R = -50$  Mev,  $r_1 = 7.5 \times 10^{-13}$  cm,  $d = 0.6 \times 10^{-13}$  cm.

<sup>d</sup> Cheston and Glassgold,  $V_R = -150$  Mev,  $r_1 = 7.09 \times 10^{-13}$  cm,  $d = 0.6 \times 10^{-13}$  cm.

is somewhat deceptive, since, when  $V_R = -35$  Mev, the  $l=11$  potential is just barely larger than the available center-of-mass energy,  $E$ , and similarly, when  $V_R = -150$  Mev, the  $l=12$  potential is just barely under  $E$ . To emphasize the similar appearance of all three potentials at the nuclear surface for the same value of angular momentum, we plot the total real potentials *versus*  $r$  for  $l=11$  in Fig. 12.

We would like to make two rather interesting side observations on the material in Table III: (a) the sharp cutoff radius,  $R_m$ , corresponding to  $l_m$  is always larger than the radius at which the  $l_m$  potential is a maximum,  $r_b$ ; this effect is due to the attractive tail of the potential. (b) We observe in cases where there has been an optical model analysis for the same element at two different energies, that, even when  $V_R$  is decreased at the lower energy while  $r_1$  remains fixed, the radii  $r_b$  and  $R_m$  are larger at the lower energy; this effect is due to the taper of the nuclear potential and the  $(1/r^2)$  dependence of the centrifugal term, a term which becomes more important at higher energies. It is this effect which is probably responsible for the experimentally observed increase in the sharp cutoff radii as the energy is decreased, a result stated at the conclusion of Sec. II and also found when the crossover recipe is used to analyze cross section *versus* energy data at four different angles for Au.<sup>13</sup> We would like to suggest that comparison of angular distributions carried out at a variety of energies just above the Coulomb barrier will provide the best means to study the tail of the nuclear potential. One notes from Table III that the nuclear potential may be as small as 1 Mev at  $r_b$ ; in other words,  $r_b$  corresponds to a distance considerably far out in the tail. We discuss these effects more quantitatively in an Appendix.

(2) Before discussing our second question, we should first emphasize that the premise of the question is true:

that the sharp cutoff model is a good approximation to optical calculations is indicated by the correspondence in predicted cross sections and by the comparisons made in the preceding paragraphs. Further, by plotting the ratio of reaction cross section to maximum possible reaction cross section,  $1 - |\eta_l|^2$ , as a function of  $l$  for an optical model giving an adequate fit of 22-Mev Ag data, Cheston and Glassgold find that there is indeed a rather rapid change from large to small absorption centered about the sharp cutoff  $l'$ .

Some qualitative discussion concerning why there should be a correspondence between the sharp cutoff model and more sophisticated calculations is presented elsewhere.<sup>13</sup> We shall not repeat these arguments here but will make two observations which are based on the behavior of the now available optical potentials at the nuclear surface.

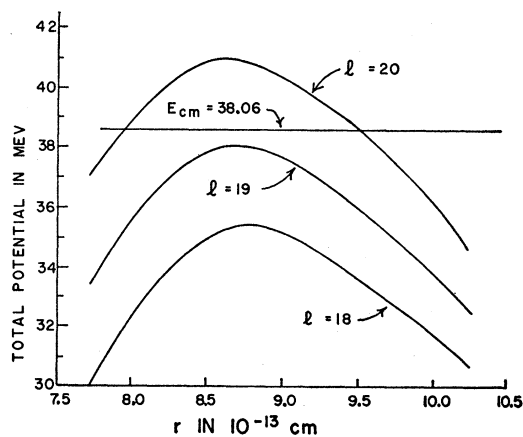


FIG. 11. Real part of total potential for 40-Mev alpha particles scattered from Ag *versus* radius near critical turning point for three values of angular momentum:  $l=18, 19, 20$ . The optical parameters of Igo and Thaler are used to provide the nuclear potential. The center-of-mass energy is 38.6 Mev.

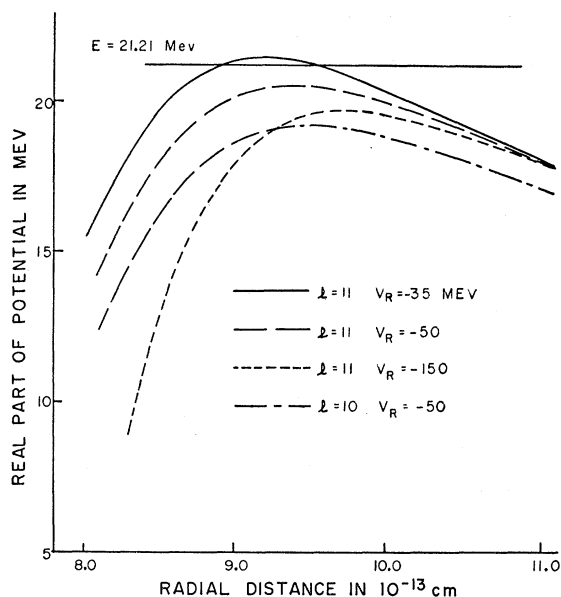


FIG. 12. Real part of total potential for 22-Mev alpha particles scattered from Ag versus radius near critical turning point for  $l=11$ . The curves represent three different sets of optical model parameters:  $V_R = -35$  Mev,  $r_1 = 7.73 \times 10^{-13}$  cm,  $d = 0.5 \times 10^{-13}$  cm;  $V_R = -50$  Mev,  $r_1 = 7.5 \times 10^{-13}$  cm,  $d = 0.6 \times 10^{-13}$  cm;  $V_R = -150$  Mev,  $r_1 = 7.09 \times 10^{-13}$  cm,  $d = 0.6 \times 10^{-13}$  cm.<sup>18</sup> For parison, it is seen that the difference between these curves near maximum is of the order of the difference between the  $-50$ -Mev curves for  $l=11$  and  $l=10$ .

If the transition between complete absorption and pure Coulomb scattering is to occur in a small range of  $l$ , not only must there be little transmission through the barrier of the partial waves with  $l > l'$  but also little reflection of the partial waves with  $l < l'$ . In the case of 40-Mev scattering from Ag, illustrated in Fig. 11, the change in barrier between  $l=l'=19$  and  $l=20$  is sufficient to cause a qualitative change in the transmission. The transmission of the  $l=20$  wave into the absorbing interior can be roughly estimated by the standard penetration factor,  $T = \exp(-2 \int \kappa dr)$ , with  $\hbar^2 \kappa^2 / 2\mu = V - E$ , and is of the order 0.1. We note that a sharp boundary condition would give a smaller value for the integral and hence larger transmission.

On the other hand, a sufficient condition that there be little reflection in the barrier region of waves with  $l < l'$  is that the WKB approximation be valid, or equivalently, that the fractional change in wavelength be small in a distance of one wavelength. It is seen again in Fig. 11 that, although the potential changes rapidly with distance for  $r$  less than  $8.0 \times 10^{-13}$  cm, the wavelength does not change by more than a factor  $\frac{2}{3}$  in the barrier region between  $r = 8.0$  and  $10.0 \times 10^{-13}$  cm for  $l \leq 18$ . For numerical orientation we mention that the wavelength of an alpha particle with 5-Mev kinetic energy is  $1 \times 10^{-13}$  cm. In this discussion of reflection, we have tacitly assumed that only the real potential contributes to the refractive index; this is not true, however, for large values of the imaginary potential,

and, indeed, there is a breakdown in the WKB condition for sufficiently large  $V_I$ . Cheston and Glassgold<sup>18</sup> have already pointed out that reflection from the surface increases with increasing  $V_I$ .

The transition between absorption and pure Coulomb scattering should be more rapid as a function of  $l$  for heavy-ion scattering than for alpha-particle scattering under comparable experimental circumstances, i.e., for the same incident velocity; one can readily show for these conditions that the transmission of the  $l'+1$  barrier decreases as the ions become heavier (for the same velocity,  $l'$  increases with the charge of the projectile) and that the WKB criterion is more easily satisfied with heavier ions since the corresponding wavelengths are smaller. The sharp cutoff model has already shown good agreement with experiment in one case of heavy-ion scattering, namely elastic scattering of  $N^{14}$  from  $N^{14}$ .<sup>22</sup>

(3) When data are analyzed in terms of a multi-parameter theory such as the optical potential model, the uniqueness of the model is almost always subject to question. Equivalently, one can ask whether there are some "effective" quantities, determined to a high degree of accuracy by the experiments, which are non-uniquely related to the parameters or models, and which therefore establish necessary conditions on the choice of parameters and models. The most recent example of such a situation is that of high-energy elastic electron scattering, where the data are most readily characterized by a mean radius and a surface thickness<sup>23</sup>; the choice between the several possible charge densities with the same mean radius and surface thickness requires great experimental accuracy.

It has already been pointed out that there is again such a lack of uniqueness when the optical model is used to describe elastic alpha scattering. Glassgold and Cheston<sup>18</sup> find that two quite different sets of parameters give adequate fits for 22-Mev alphas on Ag, while Igo and Thaler<sup>19</sup> observe that not significantly worse fits were obtained when the usual Saxon-Woods radial dependence was altered so that the imaginary potential was weighted at larger distances. Can we now find "effective" quantities in the case of alpha scattering analogous to those mentioned in the preceding examples?

We would like to suggest, on the basis of the discussion in Secs. (1) and (2), that, when the penetration depth of the bombarding particle is small, the most important "effective" quantity is  $l_m$ , which for the Saxon-Woods potential is a function of  $r_1$ ,  $d$  and  $V_R$ . Further, from the optical analysis of the data well below the break, we guess that the next most important parameters are  $d$  (or perhaps  $dV_R/dr|_{r_1}$ ) and some mean penetration depth relative to  $R$  for partial waves with  $l < l_m$ .

<sup>22</sup> H. L. Reynolds and A. Zucker, Phys. Rev. **102**, 1378 (1956).

<sup>23</sup> D. G. Ravenhall and D. R. Yennie, Phys. Rev. **88**, 277 (1955).

Since these quantities are properties of the nuclear surface, we see that the primary role of the full optical model is to furnish a means for describing the surface, i.e., the scattering depends on the interior quantities,  $V_R$ ,  $V_I$  and even  $r_1$ , only insofar as they affect the surface. The scattering should be particularly insensitive to  $V_R$ <sup>18</sup> because of the manner in which it determines  $l_m$ ; a large change in  $V_R$  can be compensated for by a small shift in  $r_1$  so long as  $d$  is small. This is in contrast to the situation found when the mean free path is of the order of nuclear dimensions: Glassgold *et al.*<sup>24</sup> observe in the case of elastic scattering of 10-Mev protons that one of the "effective" quantities is  $V_R r_1^2$ . Another corollary of the surface point of view is that the usual expression for mean free path in the nuclear interior is not necessarily a relevant quantity; the larger share of absorption probably occurs before the interior is reached. It should be possible to determine definitively where the absorption occurs by inspection of the radial dependence of the complex-potential radial wave functions which have already been computed.

In summary, the prime lesson of the present comparison between the sharp cutoff and optical models, is that the scattering of alpha particles is primarily determined by the aspect of the nuclear surface.

#### ACKNOWLEDGMENTS

We wish to thank Dr. D. Newton for his assistance in setting up the computations on the University of Washington IBM 604 computer, Mr. P. Stevens and Mr. F. Major for their computational aid, Dr. Ellis, Schechter, Gove, Wegner, Eisberg, Igo, Thaler, Cheston, and Glassgold for furnishing us with large-scale graphs of their data and informing us of their results prior to publication, and many members of the Department of Physics at the University of Washington for helpful criticism.

#### APPENDIX. ENERGY OR ANGULAR DEPENDENCE OF $R$

We may express the observations (a) and (b) of the discussed section, III (1), more fully with the help of the following short analysis. For the case of a tapered nuclear potential,  $V_{\text{nucl}}$ , let us suppose that the critical angular momentum,  $l'$ , (treated here as a continuous variable) is determined by the joint requirement that the total potential equal the available energy when the potential is a maximum, i.e.,

$$E = V(r_b) = \frac{ZZ'e^2}{r_b} + \frac{\hbar^2 l'(l'+1)}{2\mu r_b^2} + V_{\text{nucl}}(r_b), \quad (\text{A-1})$$

<sup>24</sup> Glassgold, Cheston, Stein, Schuldt, and Erickson, Phys. Rev. **106**, 1207 (1957).

and

$$\left. \frac{dV}{dr} \right|_{r_b} = 0 = -\frac{1}{r_b} \left( \frac{ZZ'e^2}{r_b} + 2 \frac{\hbar^2 l'(l'+1)}{2\mu r_b^2} \right) + \left. \frac{dV_{\text{nucl}}}{dr} \right|_{r_b}. \quad (\text{A-2})$$

For an attractive nuclear potential whose magnitude is exponentially decreasing at the surface with  $(1/e)$  distance  $d$ ,

$$\frac{dV_{\text{nucl}}}{dr} = -\frac{1}{d} V_{\text{nucl}}. \quad (\text{A-3})$$

With the assumption that  $(R-r_b) \ll r_b$ , we can eliminate  $l'$  and  $r_b$  in Eqs. (1), (A-1), and (A-2) and find  $(R-r_b) = d$ ; in words, the sharp cutoff radius corresponding to  $l'$  is larger than the radius at the top of the  $l'$ th barrier by the value of the surface parameter.

To understand the second observation, let us first denote  $r_{b0}$  as the value of  $r_b$  at threshold energy,  $E_0$ , defined by  $l'=0$ . We note that for threshold energy, Eq. (A-2) gives

$$E_0 = -\left( \frac{r_{b0}}{d} - 1 \right) V_{\text{nucl}}(r_{b0}), \quad (\text{A-4})$$

so that the nuclear potential will be quite small at  $r_{b0}$ . On the assumption that the nuclear potential is not velocity dependent, we manipulate the above equations to obtain the following approximate expression for  $r_b$  corresponding to center-of-mass energy  $E$

$$r_b = r_{b0} - d \ln \left( \frac{2E}{E_0} - 1 \right). \quad (\text{A-5})$$

If the crossover or one-quarter-point recipes are used to determine  $R$ , Eq. (A-5) leads to

$$R = R_0 - d \ln[\csc(\phi/2)]. \quad (\text{A-6})$$

It is interesting to see what changes in this analysis result when we relax the condition stated by Eq. (A-1). If we assume that  $l'$  is the critical angular momentum for which the available energy surpasses the total potential at the top of the barrier by an amount  $\delta E$ , then the energy dependence expressed by Eq. (A-4) is essentially unchanged but

$$R = r_b + d \left( 1 + \frac{\delta E}{V_{\text{nucl}}(r_b)} \right). \quad (\text{A-7})$$

The further assumption that  $\delta E$  is half the energy separation between the  $l'$ th and  $(l'+1)$ th barriers, an assumption which is not inconsistent with the correspondence of  $l'$  and  $l_m$  in Table III, leads to

$$R = r_b + d \left[ 1 - \frac{(20)^{\frac{1}{2}} (E - E_0)^{\frac{1}{2}}}{d (2E - E_0)} \right], \quad (\text{A-8})$$

when  $E$  is expressed in Mev,  $d$  in  $10^{-13}$  cm. The difference,  $(R - r_b)$ , then equals  $d$  only at  $E_0$ ; for  $1.1 E_0$

$\langle E \rangle < 3 E_0$ , the difference is practically constant and, for the case of  $Pb$  and  $d = 0.5 \times 10^{-13}$  cm, is of the order  $0.20 \times 10^{-13}$  cm. On the other hand the assumption that  $\delta E$  be constant would require

$$R = r_b + d \left[ 1 - \left( \frac{r_b}{d} \right) \left( \frac{\delta E}{2E - E_0} \right) \right]. \quad (\text{A-9})$$

Our uncertainty regarding these various assumptions and further, the result from optical analyses<sup>19</sup> that the nuclear potential itself appears energy dependent, cause us to refrain from using the above equations to correct the data. Nonetheless we think the analysis does provide a qualitative understanding of the observed angular and energy dependence of  $R$ .

## Transition in 26-min $U^{235m}$ of Less Than 23 Electron Volts

M. S. FREEDMAN, F. T. PORTER, F. WAGNER, JR., AND P. P. DAY  
Argonne National Laboratory, Lemont, Illinois

(Received July 22, 1957)

The conversion electron spectrum from the decay of 26-min  $U^{235m}$  has been examined by both magnetic spectrometry employing preacceleration and by electrostatic spectrometry. The energy distribution is peaked at 0.5 electron volts, with evidence of structure at 5 ev and at 19 ev, leading to an estimated upper limit of 23 ev for the transition energy. Tests of the performance of the apparatus were made with the conversion spectrum of the low-energy transition in 6-hr  $Tc^{99m}$ , redetermined as 2.15 kev; with the "zero energy" peak of  $Am^{241}$  and with the spectrum of photoelectrons excited from silver with ultraviolet light.

### I. INTRODUCTION

THE existence of a very low-energy isomeric state in  $U^{235}$  following the unhindered 5.150-Mev  $\alpha$  decay of  $Pu^{239}$  ( $\frac{1}{2}+$ ) was recently discovered independently by Huizenga *et al.*<sup>1</sup> and by Asaro and Perlman.<sup>1</sup> The  $26.16 \pm 0.03$  min isomeric decay<sup>2</sup> is thus expected to go by an  $E3$  transition from a presumed  $\frac{1}{2}+$  state to the (measured)  $\frac{7}{2}-$  ground state of  $U^{235}$ .

That the very soft radiation was indeed coming from  $U^{235m}$  was established<sup>1</sup> both by chemical separation of uranium from  $Pu^{239}$  and by observing the decay of electrostatically collected recoils from the  $Pu^{239}$   $\alpha$ -decay. The radiation is detectable in a windowless Bradley PCC-11 proportional counter, which has, for this activity, a plateau 75 volts long of slope 10% per 100 volts. At the upper end of this plateau the counting rate exceeds 50% of the  $\alpha$  counting rate (in  $2\pi$  geometry) of the parent  $Pu^{239}$  sample from which the recoils are collected. This lower limit on the counter efficiency corresponds, as will be shown, to the counting of single electrons of energy less than 19 ev ejected per decay event. Identification of the radiation as very weak electrons was established by the observation that an absorbing film of  $\sim 2 \mu\text{g}/\text{cm}^2$  of Formvar laid in intimate contact with the sample backing ranged out the count completely. For quanta above 1 ev such an absorber is over 90% transparent.

The first actual energy determination was made<sup>3</sup> in an internal sample proportional spectrometer in which

it was shown that the pulse-height distribution from  $U^{235m}$  was nearly identical with that from single low-energy photoelectrons ejected from the wall of the counter with ultraviolet light. In the work reported here by magnetic and electrostatic spectrometry the radiation is seen to possess the magnetic rigidity and energy characteristic of negative electrons distributed in energy in the range 0-19 ev, peaked sharply at 0.5 volt.

### II. SOURCE PREPARATION

Electrostatic collection of charged recoils from the  $\alpha$  emission in  $Pu^{239}$  was used for preparing essentially weightless sources for this study. An "emanating" film of 8 mg of  $Pu^{239}$  evaporated on about 200  $\text{cm}^2$  of 1-mil Al foil folded into a 4-inch diameter cup constituted

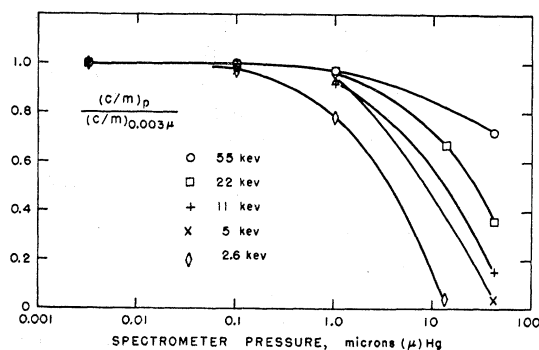


FIG. 1. The effect of spectrometer pressure on electron lines of various energies. The ordinate is the counting rate at any pressure relative to that at  $0.003 \mu$  Hg. The path length in the spectrometer is about one meter. The source of conversion lines is  $Am^{241}$ .

<sup>1</sup> Huizenga, Rao, and Engelkemeir, *Phys. Rev.* **107**, 319 (1957); I. Perlman (private communication).

<sup>2</sup> J. R. Huizenga (private communication).

<sup>3</sup> D. W. Engelkemeir (private communication).